Laser microsculpting for the generation of robust diffractive security markings on the surface of metals

Wlodarczyk, Krystian; Ardron, Marcus; Waddie, Andrew John; Dunn, Andrew; Kidd, Matthew; Weston, Nick J.; Hand, Duncan Paul

Published in:
Journal of Materials Processing Technology

DOI:
10.1016/j.jmatprotec.2015.03.001

Publication date:
2015

Citation for published version (APA):
Wlodarczyk, K. L., Ardron, M., Waddie, A. J., Dunn, A., Kidd, M., Weston, N. J., & Hand, D. P. (2015). Laser microsculpting for the generation of robust diffractive security markings on the surface of metals. Journal of Materials Processing Technology, 222, 206-218. 10.1016/j.jmatprotec.2015.03.001

Title: Laser microsculpting for the generation of robust diffractive security markings on the surface of metals

Author: Krystian L. Wlodarczyk Marcus Ardron Andrew J. Waddie Andrew Dunn Matthew D. Kidd Nicholas J. Weston Duncan P. Hand

PII: S0924-0136(15)00088-6
DOI: http://dx.doi.org/doi:10.1016/j.jmatprotec.2015.03.001
Reference: PROTEC 14311

To appear in: *Journal of Materials Processing Technology*

Received date: 7-9-2014
Revised date: 22-1-2015
Accepted date: 3-3-2015

Please cite this article as: Wlodarczyk, K.L., Ardron, M., Waddie, A.J., Dunn, A., Kidd, M.D., Weston, N.J., Hand, D.P.,Laser microsculpting for the generation of robust diffractive security markings on the surface of metals, *Journal of Materials Processing Technology* (2015), http://dx.doi.org/10.1016/j.jmatprotec.2015.03.001

Laser microsculpting for the generation of robust diffractive security markings on the surface of metals

Krystian L. Wlodarczyk[a,*], Marcus Ardron[a,b], Andrew J. Waddie[a], Andrew Dunn[a],
Matthew D. Kidd[b], Nicholas J. Weston[b] and Duncan P. Hand[a]

[a] Institute of Photonics and Quantum Sciences, School of Engineering and Physical Sciences, Heriot-Watt University, Edinburgh, EH11 4AS, United Kingdom

[b] Renishaw plc, Research Park North, Riccarton, Edinburgh, EH14 4AP, United Kingdom

[*]Corresponding author: Krystian L. Wlodarczyk

Room EM G24, Heriot-Watt University, Riccarton, Edinburgh, EH14 4AS, UK

Email address: *K.L.Wlodarczyk@hw.ac.uk*

Telephone: 0044 (0) 131 451 3105

Abstract

We report the development of a laser-based process for the direct writing (‘*microsculpting*’) of unique security markings (reflective phase holograms) on the surface of metals. In contrast to the common approaches used for unique marking of the metal products and components, e.g., polymer holographic stickers which are attached to metals as an adhesive tape, our process enables the generation of the security markings directly onto the metal surface and thus overcomes the problems with tampering and biocompatibility which are typical drawbacks of holographic stickers. The process uses 35 ns laser pulses of wavelength 355 nm to generate optically-smooth deformations on the metal surface using a localized laser melting process. Security markings (holographic structures) on 304-grade stainless steel surface are fabricated, and their resulted optical performance is tested using a He-Ne laser beam of 632.8 nm wavelength.

Keywords

Laser materials processing

Surface modification

Microstructure fabrication

Diffractive optics

Laser marking

Metals

1. Introduction

Laser-based melting processes are increasingly used in a variety of industrial (Wissenbach *et al.*, 2011), medical (Temmler *et al.*, 2010) and optical (e.g. Nowak *et al.*, 2006) applications for surface smoothing and polishing. In these processes, the laser beam is used to generate a melt pool on the material surface, enabling the molten layer to flow under surface tension forces, thereby causing surface relaxation and consequently roughness reduction (Wlodarczyk *et al.*, 2010). Typically, however, new surface deformations such as bumps, dimples, corrugations and ripples are also generated during the re-melting and re-solidification process. The appearance of such surface deformations depends on the absorbed laser intensity, temperature gradients generated on the surface and the chemical composition of the material, as explained by Wissenbach *et al.* (2011). Chen *et al.* (2009), for instance, observed that deformations in the form of bumps generated on a Ni-P hard disk substrate result from both a change in the surfactant concentration and the thermocapillary (Marangoni) forces which are induced by the temperature gradients occurring across the molten area.

Fibre and solid-state lasers are commonly used for re-melting, polishing and texturing the surface of metals, such as steel (Tammler *et al.*, 2011), titanium (Nusser *et al.*, 2013), GGG70L cast iron (Ukar *et al.*, 2013) and nickel-based Inconel$^{®}$718 alloy (Kumstel *et al.*, 2013). Khoong *et al.* (2010) demonstrated that a 355nm solid-state YAG laser can also be used for so called “soft marking” of silicon wafers. In the case of transparent materials, such as glass and glass-ceramics, surface polishing and texturing processes are carried out by using a CO_2 laser beam at 10.6 µm because at this wavelength these materials have a high absorption coefficient, enabling the laser light to be coupled more efficiently. For example, it has been demonstrated that a CO_2 laser beam can be successfully used for polishing the surface of conventional refractive optic (Laguarta *et al.*, 1994 and Heidrich *et al.*, 2011) and for smoothing sharp etched-edges of diffractive optical elements (Wlodarczyk *et al.*, 2010). The CO_2 laser irradiation can also be used for the fabrication of micro-optical components, e.g., micro-stripe cylindrical and toroidal mirrors (Wlodarczyk *et al.*, 2012) and phase corrective plates for high power laser diodes, as reported by Nowak *et al.* (2006), Monjardin *et al.* (2006) and Trela *et al.* (2009). A CO_2 laser beam can also be used for texturing the surface of optical glasses, as demonstrated by Shiu *et al.* (1999) and Bennett *et al.* (1999), or even for repairing of damage in fused silica components by re-melting, as reported by Mendez *et al.* (2006) and Cormont *et al.* (2013). Moreover, Brusasco *et al.* (2001) and recently Dai *et al.* (2011) demonstrated that CO_2 laser polishing can also enhance surface damage resistance of optical components.

Currently common techniques for marking metals include mechanical processes (e.g. indentation), ink-marking, laser ablation (marking and engraving), electro-marking and etching, which are typically used for the generation of company logos, trademarks, alphanumeric characters (e.g. serial numbers), bar codes, QR codes and data matrices (Dahotre and Harimkar, 2008). All these ‘standard’ markings, however, can be easily replicated and thus expensive products (e.g. engine components) can be counterfeited. More sophisticated markings like polymer holographic stickers, which are more robust to local damage and counterfeiting, are produced by a mechanical embossing process. Such holograms, however, are not embedded into the metal surface, but rather attached as an adhesive tape, and thus are vulnerable to tampering. Moreover, they reveal biocompatibility problems and thus they cannot be used for marking medical instruments and implants.

The work described in this paper is focused on the development of a process for the generation of small-scale surface features (with a diameter of up to 10 μm and a peak-to-valley value of up to 500 nm) on metals using a localised laser melting process. By creating the deformations in appropriate locations on the metal surface, we generate optically-smooth holographic structures which are directly embedded into the metal. Since such structures can produce a diffraction pattern containing text and images, they simply can be used as security markings for identification and traceability of high value metal components. In this paper, we investigate the generation of laser-induced surface deformations (LISDs) in metals which are commonly used as substrates for manufacturing medical instruments, implants and components in aircraft engines, nuclear reactors and pumps. The LISDs are generated by a pulsed, frequency-tripled solid-state laser which provides 35 ns pulses at a 10 kHz pulse repetition frequency in UV ($\lambda = 355$ nm). Based on our previous work, which was reported by Weston *et al.* (2012), this laser is capable of producing optically-smooth deformations with the peak-to-valley value of 200±20 nm on the surface of different metals, such as a 316-grade stainless steel and martensitic chromium steel Sandvik Chromflex®. In this paper, we analyse the evolution of the LISDs in terms of the applied laser pulse energy (average power) and the number of laser pulses and identify the laser processing parameters which can be used to generate optically-smooth surface features with a good control over their depth or height.

2. Interaction of UV nanosecond laser pulses with metals

Four different metals, austenitic 304-grade stainless steel, 99% pure nickel and two nickel-chromium alloys (Inconel®625 and Inconel®718 alloy) were investigated. The stainless steel samples were 0.35 mm thick, whereas the thickness of the other samples was 2 mm. The metal surfaces were mechanically polished before the laser treatment. The metal samples after polishing were measured to have an average surface roughness Ra < 6 nm and RMS (Rq) < 10 nm in a 0.34 mm by 0.26 mm measured window.

A detailed analysis of the laser-induced surface deformations (LISDs) generated by the nanosecond pulses in UV was performed using a white-light source interferometer (Zygo) and an atomic force microscope (Digital Instruments Veeco). These instruments measured the LISDs with a lateral (spatial) resolution of < 0.2 μm and a vertical resolution of ≤ 1 nm. Based on the surface profiles, the diameter, peak-to-valley value and level (depth/height) of the central area of the LISDs were determined for different values of the pulse energy (average laser power) and number of laser pulses.

2.1. *Experimental setup*

The optical setup used in the experiments described below is shown in Figure 1. The laser source is a 10 W Q-switched diode-pumped UV laser (JDSU Q-series) which provides 35 ns pulses (FWHM) with a 10 kHz pulse repetition frequency. A 1.6 mm diameter laser beam (measured at $1/e^2$ of its maximum intensity) with $M^2 < 1.2$ is delivered to the workpiece via a half-wave ($\lambda/2$) plate, polarising beam splitter (PBS) cube, a ×3 beam expander (BEX) and a conventional plano-convex (PCX) spherical lens of 50 mm focal length. The focused laser beam diameter on the workpiece ($2\cdot\omega_o$) was calculated to be 8±1 μm (at $1/e^2$ of its maximum intensity) using the following equation:

$$\omega_o = \frac{M^2 \cdot FL \cdot \lambda}{\pi \cdot \omega_I}, \qquad \text{(Eq. 1)}$$

where *FL* is the focal length of the PCX spherical lens (50 mm), λ is the laser wavelength (355 nm), and ω_I is the radius of the expanded laser beam which was measured to be 2.6 mm (at $1/e^2$ of its maximum intensity). The M^2 value of the laser beam after BEX was measured to be approximately 1.8. The calculated focused laser beam diameter is similar to the diameter of LISDs observed in the studied metals (see Sections 2.2 – 2.5). It was not possible to directly measure the focused laser beam using a beam-profiling camera (e.g. Spiricon) because the laser spot size is similar to the camera resolution.

Laser processing is carried out by moving the workpiece using two motorised linear stages. When the workpiece is settled in a desired position, the laser delivers a pre-defined number of laser pulses at fixed energy to the target. The stages ensure the workpiece movement with a 0.5 μm resolution. The maximum average laser power (pulse energy) delivered to the workpiece was manually controlled by rotating the $\lambda/2$ plate, whereas very accurate adjustment (with a 1% resolution of the maximum average power) was carried out using the laser software.

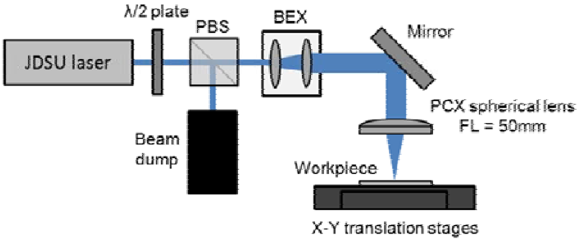

Figure 1. Schematic of the experimental setup.

2.2. *304-grade stainless steel*

Austenitic 304-grade stainless steel is the most versatile and widely used stainless steel. This metal contains at least 66% Fe, 17.5 – 19.5% Cr, 8 – 10.5% Ni, up to 2% Mn, up to 1% Si and some traces of C, P and S.

In general, it was found that the UV ns laser pulses generate repeatable and useful structures on the 304-grade stainless steel. This was not the case for the longer wavelengths (1030 nm and 515 nm) where the degree of depth control is much reduced and the generated surface is significantly rougher. In the range of laser pulse energies (E_p) between 1.5 and 4.5 µJ, the LISDs were observed in the form of smooth '*Gaussian-like*' craters with an elevated rim. Figure 2 shows examples of such deformations. Craters with a depth of > 0.7 µm were produced when $E_p > 4.5$ µJ. Such deep craters are not discussed further because they are beyond the scope of our interest.

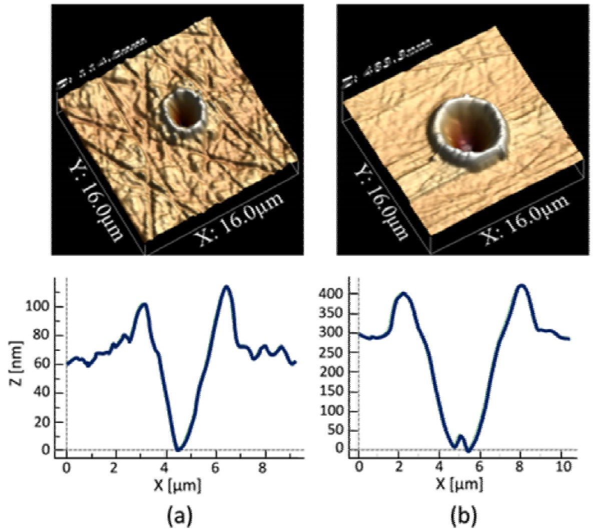

Figure 2. Laser-induced deformations (LISDs) produced on the surface of 304-grade stainless steel. LISDs were generated by single laser pulses at: (a) $E_p = 1.5$ µJ and (b) $E_p = 2.75$ µm.

AFM analysis reveals that the depth of the LISDs (craters) increases in an almost linear manner with increasing laser power for single laser pulses, as can be seen in Figure 3 (a). Single laser pulses with energies in the range of 1.0 – 4.5 µJ hence provide good deformation depth control. For multiple laser pulses, meanwhile, the depth of the craters was found to change only by less than 20% in comparison to those generated by single laser pulses in the range of pulse energies between 1.5 and 3.0 µJ, as can be seen in Figure 3 (b). This is because no vaporisation occurs in this regime, only melting.

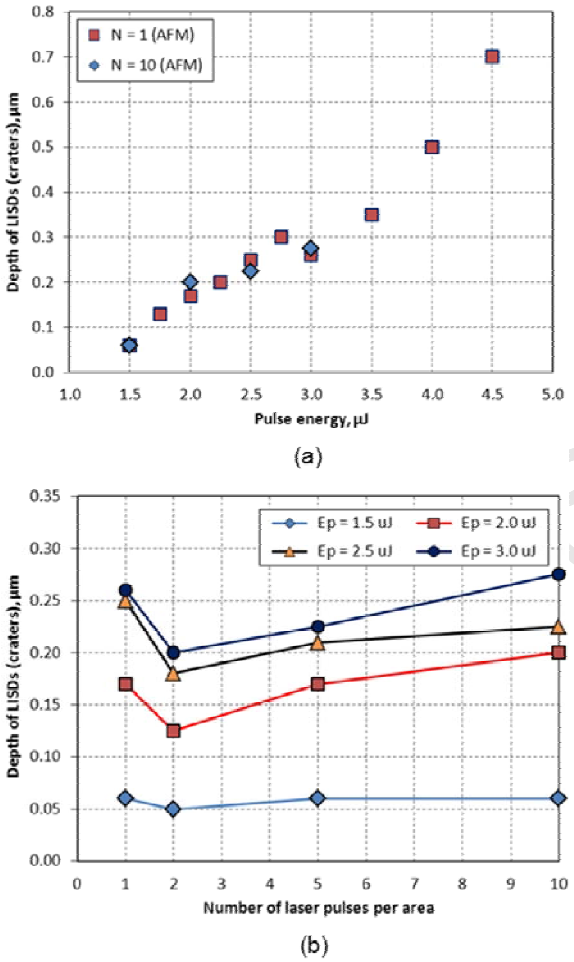

Figure 3. Depth of the LISDs (craters) in 304-grade stainless steel as a function of (a) laser pulse energy and (b) number of laser pulses.

2.3. *99% pure nickel*

The onset of the LISDs in the 99% pure nickel sample was found at E_p = 1.2 µJ, i.e. a similar pulse energy level to which the onset of the LISDs was observed in the 304-grade stainless steel sample. However, the response of the nickel surface to the UV nanosecond laser pulses was significantly different. Simple '*dome-shaped*' bumps were generated by both single and multiple laser pulses in the range of E_p between 1.6 and 2.0 µJ, whereas more complex (so called '*sombrero-shaped*') bumps were produced only by multiple laser pulses with E_p in the range of 1.4 – 2.8 µJ. '*Gaussian-like*' craters were also generated using single laser pulses with E_p in the range of 2.4 – 3.6 µJ. Figure 4 shows examples of the LIDS produced on the surface of the nickel sample.

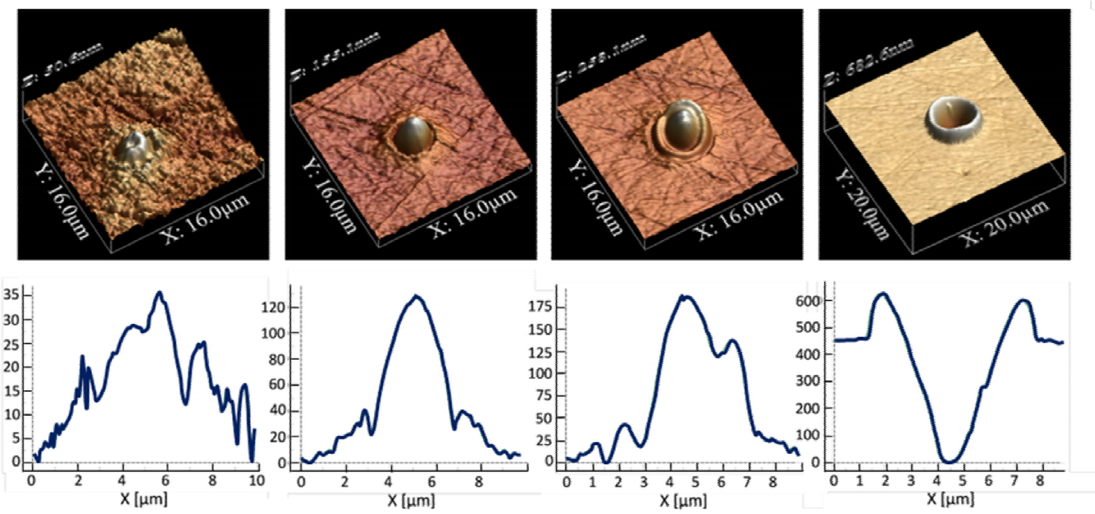

(a) (b) (c) (d)

Figure 4. LISDs generated on 99% pure nickel. The deformations were produced using the following laser processing parameters: (a) E_p = 1.6 μJ, 1 pulse, (b) E_p = 1.6 μJ, 10 pulses, (c) E_p = 2.4 μJ, 10 pulses, (d) E_p = 3.2 μJ, 1 pulse.

Figure 5 shows the changes in the level of the central area of the LISDs for the nickel sample when treated by different pulse energies and numbers of pulses. The results clearly show that it is difficult to accurately control the depth/height of the deformations in this material. However, it is still feasible to produce optically-smooth surface deformations such as:

a) '*Gaussian-like*' craters with a depth of > 50 nm using single laser pulses in the range of E_p between 2.4 and 3.6 μJ – see Figure 5 (a),

b) '*dome-shaped*' bumps with a height of up to 300 nm using multiple laser pulses ($N \geq 5$) and pulse energies between 1.6 and 2.0 μJ – see Figure 5 (b).

Both of these types of the LISDs can be potentially used for the generation of security marking (holograms) on the surface of nickel-made components.

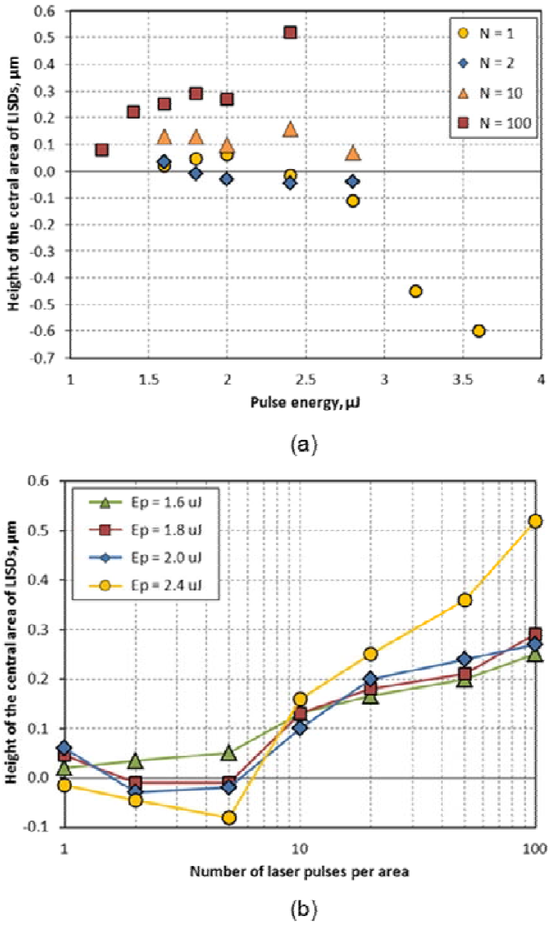

Figure 5. The height of the central area of the LISDs in 99% pure nickel as a function of (a) laser power and (b) number of laser pulses.

2.4. *Inconel*$^{®}$*625 alloy*

Inconel$^{®}$625 is a nickel-chromium alloy that contains at least 58% Ni, 20-23% Cr, 8-10% Mo, up to 5% Fe, 3-4% Nb and less than 1% C, Mn, Si, P, S, Al, Ti and Co. Due to outstanding corrosion resistance, excellent thermo-mechanical properties, high tensile, creep and rupture strength, this material has found use in sea-water applications (e.g. mooring cables, propeller blades) and aerospace (e.g. aircraft ducting and engine exhaust systems).

As with the 99% pure nickel sample (see Section 2.3), Inconel$^{®}$625 alloy was found to produce bumps rather than craters when processed with the laser. This is probably because this alloy contains a relatively large amount of nickel. The onset of the LISDs in Inconel$^{®}$625 alloy was found to occur at E_p = 1.6 µJ for a single laser pulse. For the pulse energies E_p < 3.2 µJ, the LISDs were observed in the form of '*sombrero-shaped*' bumps, as shown in Figure 6 (a), whereas for energies between 3.2 and 4.4 µJ the deformations were similar in shape to the craters with a '*W-shaped*' bottom, as presented in Figure 6 (b). By applying more laser pulses, however, it was possible to flatten the '*W-shaped*' bottom, as shown in Figure 6 (c). For pulse energies above 4.4 µJ, '*Gaussian-like*' craters were created with depths greater than 0.5 µm. A very interesting case was the appearance of a '*keyhole*' in the LISDs when generated by a single laser pulse of energy $E_p \approx 4.8$ μJ, as shown in Figure 6 (d). This repeatable keyhole fortunately can be removed by subsequent laser pulses and the LISD can be transformed into a crater with the '*W-shaped*' bottom – similar to that shown in Figure 6 (c).

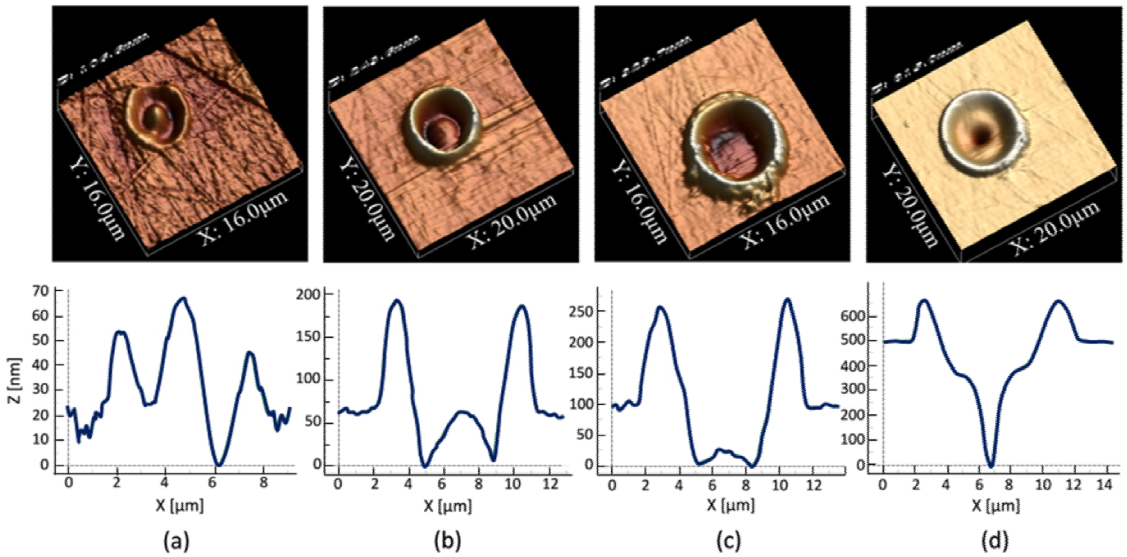

(a) (b) (c) (d)

Figure 6. Laser-induced deformation profiles observed on the surface of Inconel®625 alloy. LISDs were produced using the following laser processing parameters: (a) $E_p = 2.4$ μJ, 1 pulse, (b) $E_p = 4.0$ μJ, 1 pulse, (c) $E_p = 4.0$ μJ, 20 pulses, (d) $E_p = 4.8$ μJ, 1 pulse.

Figure 7 shows that the level of the central area of the LISDs can be changed in the Inconel®625 alloy by delivering: (a) higher energy pulses and (b) more laser pulses to the metal surface. However, due to the appearance of complex shapes in the LISDs accurate control of the height/depth values seems to be restricted to a very narrow range of pulse energies near 4.0 μJ at which the craters with a '*W-shaped*' bottom can be produced. The depth of these craters without changing their overall shape can be increased by applying more laser pulses, as can be seen in Figure 7 (b). We believe that these laser processing parameters could be used for the generation of security marking on the surface of Inconel®625 alloy.

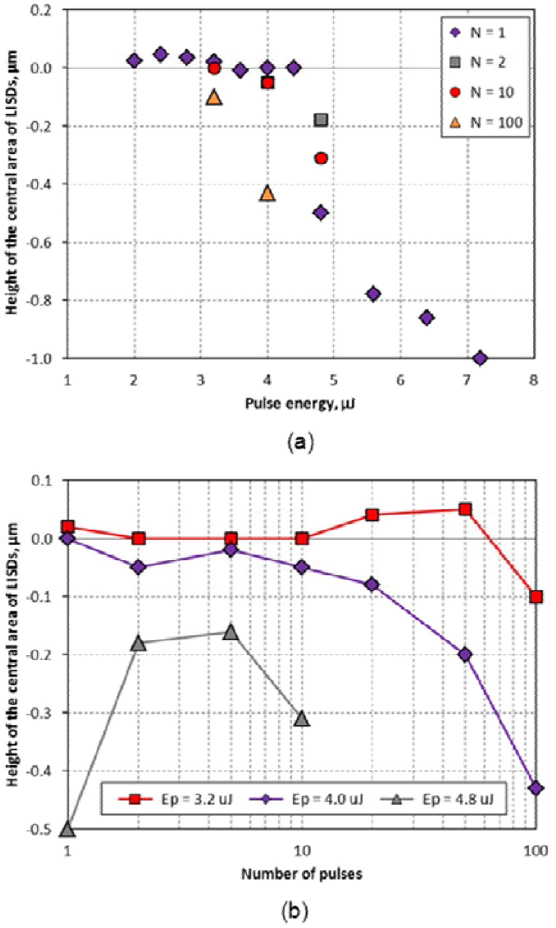

Figure 7. The height of the central area of the LISDs in Inconel®625 alloy as a function of (a) pulse energy and (b) number of laser pulses.

2.5. *Inconel®718 alloy*

Inconel®718 alloy is a high-strength, corrosion-resistant nickel-chromium material that contains 50-55% Ni, 17-21% Cr, approximately 19% Fe, 5% Nb, 3% Mo, up to 1% Ti, Al, Co, and some traces of C, Mn, Si, P, S, B and Cu. Due to its outstanding thermo-mechanical properties, this alloy is used in the field of gas turbine components, jet engines, rocket motors, pumps and nuclear reactors.

The onset of LISDs in the Inconel®718 alloy sample was found at $E_p \approx 1.4$ µJ. At pulse energies slightly above the threshold value ($E_p = 1.6$ µJ), '*Gaussian-like*' craters were created, as can be seen in Figure 8 (a), whereas for energies in the range of 2.0 – 4.0 µJ '*W-shaped*' craters were formed, as shown in Figure 8 (b). The characteristic keyhole within the laser-irradiated area, which can be seen in Figure 8 (d), was also generated with the Inconel®718 alloy sample when processed by a single laser pulse but at a slightly higher pulse energy (i.e. $E_p \approx 4.4$ µJ). The use of pulse energies above 4.4 µJ resulted in the appearance of "*Gaussian-like*" craters with depths > 0.8 µm.

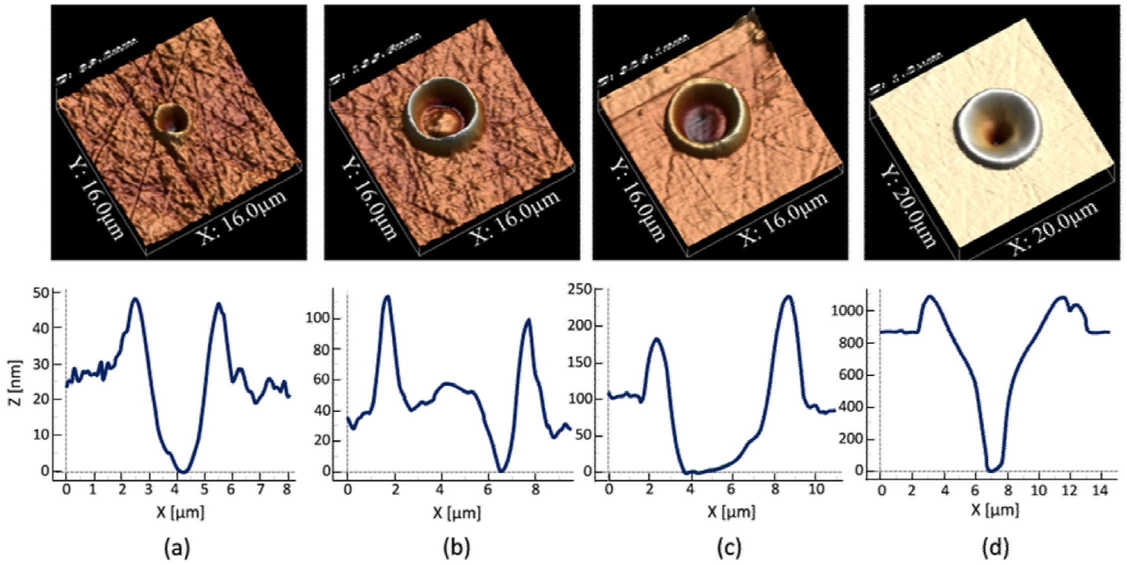

Figure 8. Laser-induced deformation profiles observed on the surface of Inconel®718 alloy. LISDs were produced using the following laser processing parameters: (a) E_p = 1.6 μJ, 1 pulse, (b) E_p = 3.2 μJ, 1 pulse, (c) E_p = 3.2 μJ, 10 pulses, (d) E_p = 4.4 μJ, 1 pulse.

Multiple laser pulses provide both an increase in the depth of the LISDs when $E_p >$ 1.6 μJ, as can be seen in Figure 9 (b), and a flattening of the '*W-shaped*' bottom of the craters, as shown in Figure 8 (c).

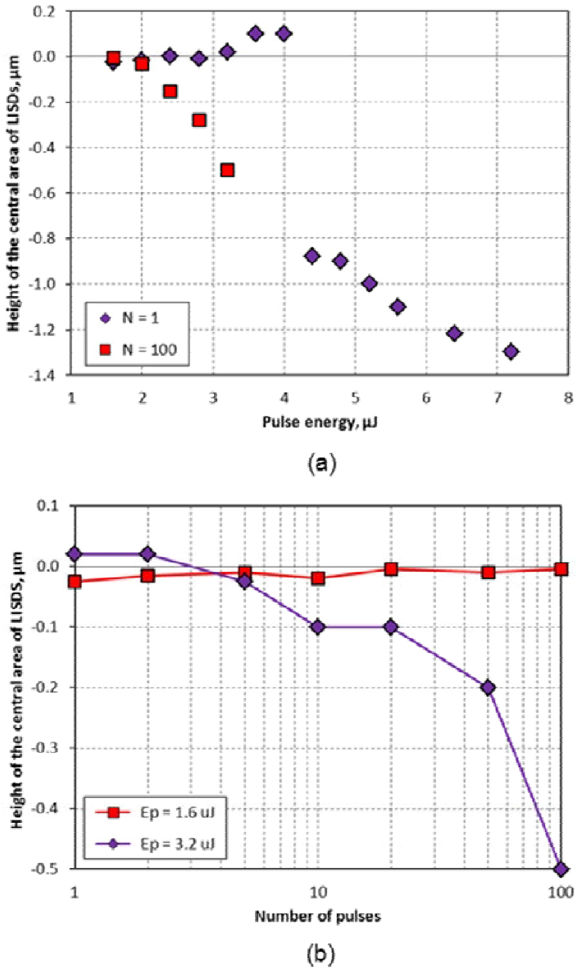

(a)

(b)

Figure 9. The height of the central area of the LISDs in Inconel®718 alloy as a function of (a) pulse energy and (b) number of laser pulses.

Based on the results presented in Figure 9, it can be concluded that the depth of the LISDs can be controlled by applying multiple laser pulses (N > 1) and pulse energies in the range of 2.4 and 3.2 µJ.

2.6. *Discussion about the laser-induced surface deformations*

The total energy (Q) that is necessary to evaporate a certain volume of a material can be estimated using the following thermodynamic equation:

$$Q = m \cdot (C_p \cdot (T_m - 20K) + L_M + C_p \cdot (T_b - T_m) + L_b), \qquad \text{(Eq. 2)}$$

where m is the mass unit (density times volume), C_p is the specific heat, T_m and T_b are the melting and vaporization temperatures, respectively, and L_m and L_b are the latent heats of melting and boiling. If we assume that the thermal properties of 304-grade stainless steel (see Table 1) are constant for increasing temperatures, then the total energy (Q) that is necessary to evaporate a 1 mm^3 volume of the steel is estimated to be 55.7 J.

Table 1. Thermal properties of 304-grade stainless steel (Cheng *et al.*, 2000)

Parameter	**Value**
Density, ρ	7900 kg m^{-3}
Specific heat, C_p	460 J $kg^{-1}K^{-1}$)
Thermal conductivity, k	17 W $m^{-1}K^{-1}$
Melting temperature, T_m	1700K
Boiling temperature, T_b	3000K
Latent heat of melting, L_m	306 kJ kg^{-1}
Latent heat of boiling, L_b	5500 kJ kg^{-1}

The pulse energy (E_p) that is necessary to initiate vaporization of the metal in our process can be estimated using the following equation:

$$E_p = Q \cdot \frac{\pi \cdot (\omega_0 + 2 \cdot L_d)^2 \cdot L_d}{A}, \qquad \text{(Eq.3)}$$

where ω_0 is the laser beam radius, A is the absorptivity and L_d is the propagation length of the heat wave over a time span equalling the duration, t_p, of the incident laser pulse (Prokhorov *et al.*, 1990). L_d is given by:

$$L_d = (\kappa \cdot t_p)^{1/2}, \qquad \text{(Eq.4)}$$

where κ is the thermal diffusivity of the metal. With 304-grade stainless steel, $\kappa = 4.7 \cdot 10^{-6}$ m^2s^{-1} (calculated from the values given in Table 1), and hence $L_d = 0.4$ µm for the 35 ns pulse used.

Equation 3 describes the plane heat model (Prokhorov *et al.*, 1990) in which the radius of the irradiated spot (ω_o) is much greater than the thermal diffusion length (L_d). This equation represents the case in which the heat wave is one dimensional and propagates into the sample perpendicularly to the sample surface. Given an absorptivity of approximately 0.6 at 343 nm (Dahotre and Harimkar, 2008), the pulse energy (E_p) which is required to initiate vaporization can be estimated to be 2.7±0.5 µJ. This value seems to agree with the experimental results shown in Fig. 3 (a), where the gradient of the plot of LISD depth as a function of pulse energy steepens for $E_p > 3$ µJ.

In general, the LISDs described in Sections 2.2 - 2.4 have been generated by either a melt-only process or a combination of melting and vaporisation, dependent on the pulse energy used. A melt-only process is possible as a result of the combination of the laser wavelength (providing a relatively high linear absorption) and pulse length (being relatively long at 35ns). Longer (green, infrared) wavelengths result in less controlled (but often stronger) material vaporisation (Leitz *et al.*, 2011), whereas shorter (picosecond) pulses leads to significant reduction of the molten area and the formation of rough laser-ablated surfaces. The evidence of pure melting on the metal surface can be clearly seen, e.g., in Figure 6 (a), and less obviously in Figure 4 (b) and (c).. The appearance of craters within the laser-irradiated area – for instance see Figure 4 (d) – means that the laser fluence was high enough to remove the material by vaporisation, whereas a surrounding rim around the craters most likely resulted from the melting effect.

In the melt-only regime, the shape of the LISDs is not always obvious and easy to explain. As described by Wissenbach *et al.* (2011), the shape depends on the temperature and temperature gradients generated by the laser beam as well as the physical and chemical properties of the metal. When a material absorbs laser radiation, a temperature gradient and convective flows are created (Von Allmen and Blatter, 1995). A Gaussian laser beam generates the highest temperature in the centre of the laser-irradiated area, forming a temperature gradient in radial direction. When the temperature exceeds the melting point of the material, convective melt flow leads to topological changes.

This flow is further complicated by the dependence of surface tension (σ) on temperature (T). For most pure metals, $d\sigma/dT < 0$ (Eustathopoulos *et. al*, 1998), including iron and steel with low content of oxygen and sulphur (Mills *et al.*, 1998). This would result in melt flow from the centre towards the edges of the pool. Sheer stresses, in turn, cause a flow of the melt along the solid-liquid interface towards the centre, and then the molten material on the bottom of the pool is drawn back towards the surface (Wissenbach *et al.*, 2011). This leads to the formation of a bump within the laser-irradiated area, like those observed in the nickel sample (see Figure 4). The appearance of bumps on the metals may also result from the fact that the rapid heating leads to fast expansion of the material.

The surface tension of iron and other elements can be substantially modified by a small change in the concentration of surface-active elements, such as sulphur and oxygen. Heiple and Roper (1982) reported that the surface tension gradient can be changed from a negative to a positive value when the sulphur or oxygen concentration exceeds a certain value (around 0.005%). Then, the surface tension is the greatest in the high-temperature region at the centre of the melt pool and this causes the melt to flow radially inwards. This, in turn, creates a downward flow in the centre of the melt pool which transfers hot metal to the bottom of the pool, forming a dimple (a crater) like that observed, e.g., in the 304-grade stainless steel sample (see Figure 2 (a)). This explanation seems valid for the stainless steel sample because this metal contains sufficient sulphur (up to 0.03%). Moreover, the melt could gain some oxygen because laser processing was carried out in air.

The '*W-shaped*' craters observed in the Inconel® alloys (e.g. see Figure 6 (a)) can be explained using the conclusions drawn by Keene *et al.* (1982) who pointed out that systems which exhibit a positive surface tension gradient must eventually go through a maximum at some temperature above which the $d\sigma/dT$ value becomes negative. Such a situation leads to a complex flow of the melt and the formation of protrusions in the centre and around the edge of the melt pool. Since both Inconel® alloys contain sulphur (less than 0.015%) and were processed in air, it seems likely that the surface tension gradient can change in this way, leading to the appearance of '*W-shaped*' craters.

3. Fabrication of security markings (holograms) on the surface of a 304-grade stainless steel

As shown in Section 2, UV nanosecond laser pulses are able to produce optically-smooth surface deformations on metals and their depth/height can be controlled by the laser power and the number of laser pulses. Such surface features, then, can be used for the generation of reflective phase holographic structures (security markings) which are more difficult to fabricate (replicate) than amplitude holographic structures which can be fabricated, e.g., by short pulse laser ablation. This is in contrast to UV picosecond laser pulses which typically produce craters with a rough (highly-scattering) base, as shown in Figure 10; also control of the depth of these surface features is rather complicated and difficult to maintain.

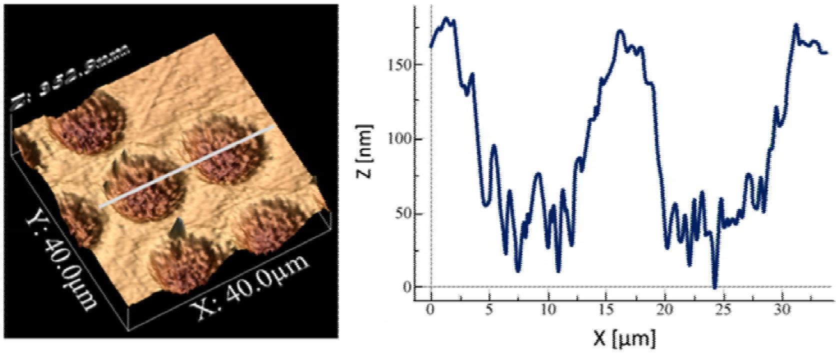

Figure 10. AFM image and surface profile of the LISDs generated in a 304-grade stainless steel. Each LISD was produced by 80 laser pulses with duration of 6 ps at a 343 nm wavelength, using a 70 mW average power and a 400 kHz pulse repetition frequency.

In this section, we describe the design and the laser-based fabrication process of unique security markings, which can be embedded directly to the surface of a metallic component or its part. As a test substrate, the same 304-grade stainless steel as that described in Section 2.2 was used.

3.1. Design of security markings

Phase Computer Generated Holograms (CGHs) are an excellent choice for use as security markings because they can carry information in the form of images, letters or both (Stepien, 2000). In order to reveal the information, the holographic structure is illuminated with coherent light and the resultant diffraction pattern is projected onto a screen. In the case of phase CGHs, it is very important to use the appropriate illumination wavelength (λ) in order to obtain the maximum diffraction efficiency (contrast) in the image generated by the hologram. For the reflective binary (two-level) CGHs, the maximum diffraction efficiency (with a lack of the 0^{th} order beam) is obtained when the phase shift is equal to λ/4.

The design of the security markings (reflective phase CGHs) has been performed using the Iterative Fourier Transform Algorithm (IFTA) described in details by Wyrowski and Bryngdahl, 1988). The algorithm, which was successfully implemented in our previous work for laser marking of metals using a spatial light modulator (see Beck *et al.*, 2010 and

Wlodarczyk *et al.*, 2014), was optimised for designing the holograms containing square-shaped individual elements (pixels). The IFTA enabled the design of both two-level and multi-level CGHs for the generation of diffractive images in the far field. By introducing more phase-shift levels in the hologram design, the diffraction efficiency of the holographic structure can be significantly increased.

3.2. Simulation of the operation of the CGHs

A mathematical model has been developed for simulating the operation of the reflective phase CGHs. The simulation is performed by implementing the Fresnel and Fraunhofer approximations (explained in Goodman, 2005) into a Matlab® (MathWorks) code to calculate the diffraction image produced by the hologram in the near-field and the far-field, respectively. The Fraunhofer approximation is used when the Fresnel number (*F*) is << 1. This number is given by:

$$F = \frac{\omega_0^2}{z \cdot \lambda}, \tag{Eq. 5}$$

where ω_0 and λ are the diameter and the wavelength of the laser beam used for illuminating the holographic structure, whilst z is the distance between the hologram surface and the projected diffraction image plane.

The model can be used for simulating the operation of both CGHs with square flat-bottom pixels, which are typically produced by the etching process, and holograms with an arbitrary pixel shape, including pixels in the form of '*Gaussian-like*' craters which can be generated on metals by UV nanosecond laser pulses, as presented in Section 2.

Figure 11 shows the simulation results obtained for a 2-level CGH and a 4-level CGH which were designed using the IFTA to generate a diffraction image containing inscription *YAGboss* and a checkerboard, as shown in Figure 11 (a). The size of the CGH pixels was 7 µm by 7 µm. In the case of the 2-level hologram, which can be seen in Figure 11 (b), the pixel depth was chosen to be 158.25 nm, corresponding to a λ/4 phase shift when λ = 633 nm. Based on the simulation results, which are presented in Figure 11 (c), this hologram generates the designed image without the zeroth order beam when it is illuminated by a 1 mm diameter beam at a 633 nm wavelength. The diffraction efficiency (η_{diff}), i.e., the fraction of the optical power in the designed image pattern shown in Figure 11 (a), was calculated to be only 26.4%. As can be seen in Figure 11 (c), the 2-level CGH in fact generates two '*twin*' target images which are rotated with respect to each other by 180 degrees. This '*twin image*' effect is a consequence of the DOE having only 2 phase levels (Freese *et al.*, 2010). Like a ruled symmetrical square grating, for example, this structure generates symmetrically positive and negative diffraction orders which form a real and conjugate image. Additional phase levels added to the holographic structure allows the symmetry to be broken in an analogous manner to a blazed grating. In the case of the 4-level CGH, whose structure is presented in Figure 11 (b), the simulation demonstrates that the hologram can generate a diffraction image which is very similar to the target image design when the depth of the pixels corresponds to the phase shift of 1/8 λ, 1/4 λ and 3/8 λ. In this case both the '*twin*' image and the 0th order beam can be completely suppressed. The diffraction efficiency (η_{diff}) for the 4-level CGH was calculated to be 53.4%. The rest of the light is scattered to the region outside the signal window used in the design of the hologram pattern.

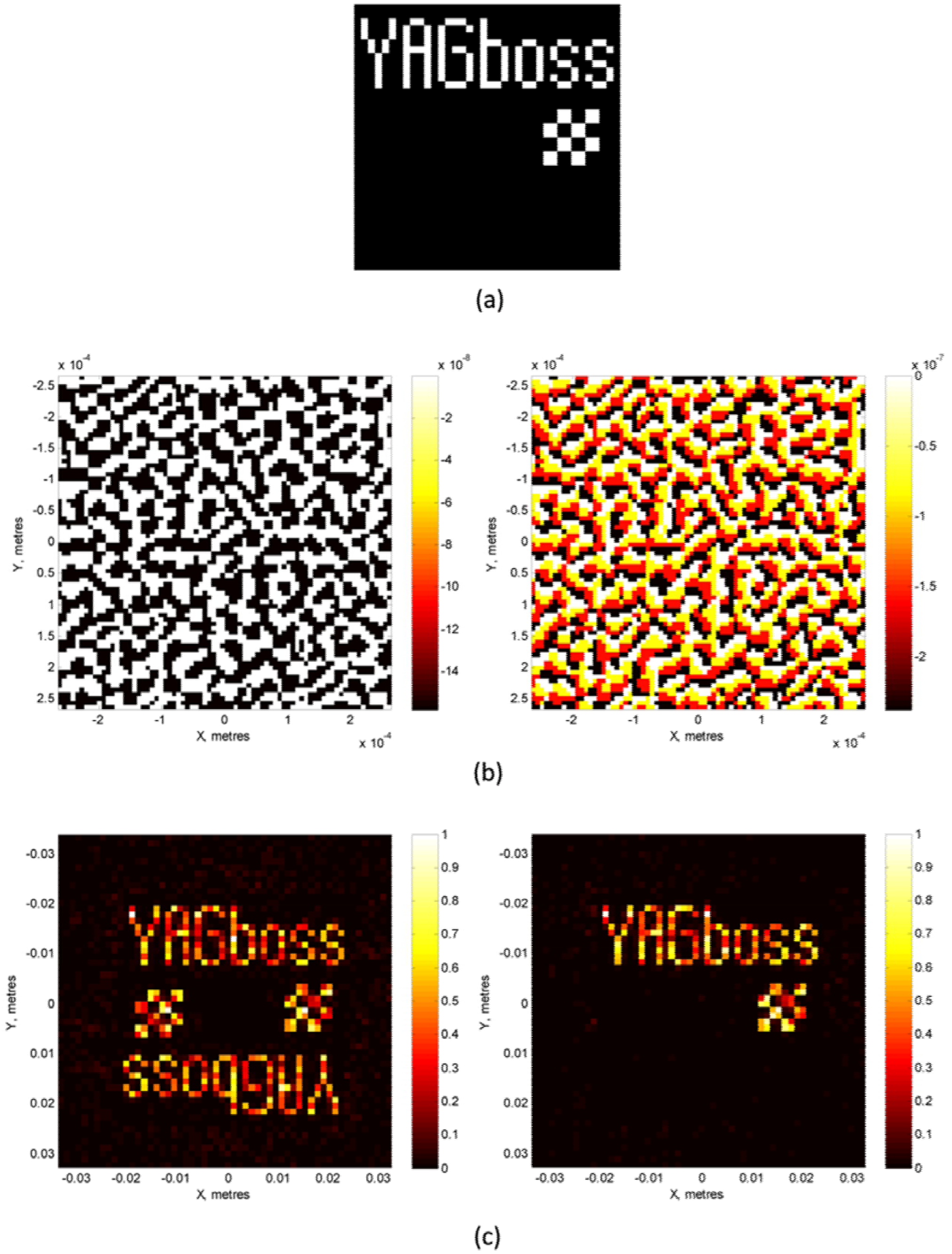

Figure 11. (a) Target image containing the inscription *YAGboss* and checkerboard, (b) 2-level CGH (left) and 4-level CGH (right) designed using IFTA, and (c) simulated diffractive image produced by the 2-level CGH (left) and 4-level CGH (right). The simulations were performed using the Fresnel approximation for a 1 mm diameter He-Ne laser beam (λ = 633 nm) and a 1 metre projecting distance.

In general, the simulations revealed that both the shape of the CGH pixels and any mismatch between the pixel depth and the laser wavelength used for illuminating the holographic structure have a significant impact on the diffraction efficiency of the hologram. For instance, when the CGH pixels have a shape of '*Gaussian-like*' craters then the hologram is still able to generate the target image but the diffraction efficiency significantly decreases due to the appearance of the 0^{th} order beam.

Figure 12 shows the simulation results obtained for both the 2-level and the 4-level CGH in which the pixels with a square contour and flat bottom were replaced by the '*Gaussian-like*' craters, like that presented in Figure 12 (a). The CGH structures are shown in Figure 12 (b), whereas the diffraction images produced by these holograms are presented in Figure 12 (c). In both cases, the CGH generated a highly intense 0^{th} order beam which suppressed the appearance of the diffraction images. In order to enhance the diffraction image contrast the intensity of the 0^{th} order beam was attenuated, dividing its intensity value by 500.

The simulations performed for the CGH structures containing '*crater-like*' pixels revealed that the 2-level hologram generates the designed image with the diffraction efficiency of only 3.7%, whilst the 4-level hologram generates the image with η_{diff} = 5.0%. Moreover, it was found that the '*twin*' image is less suppressed by the 4-level holographic structure containing '*crater-like*' pixels, as can be seen in Figure 12 (c).

Finally, it can be concluded that not only the depth of the CGH pixels but also their shape is very important in terms of the achievable diffraction efficiency and also the contrast ratio between the diffraction image and the 0^{th} order beam. It is well known from diffraction optics theory that the shape of the single diffractive element (pixel) defines an envelope of the diffraction pattern, whereas the separation between the single diffractive elements defines an angular distribution of minima/maxima in the whole diffraction pattern (Goodman, 2005). Therefore, it can be expected that the holographic structures (security markings) produced by the UV nanosecond laser pulses will not generate the diffraction images with a high contrast ratio even though the surface features, i.e. 'crater-like' pixels, will be optically smooth. Wyrowski (1991) calculated that 2D phase-only DOEs can provide a diffraction efficiency of up to 90%. Such optics, however, contain individual elements (pixels) in the form of flat-bottom squares, which typically are produced by photolithography and etching (Goodman, 2005).

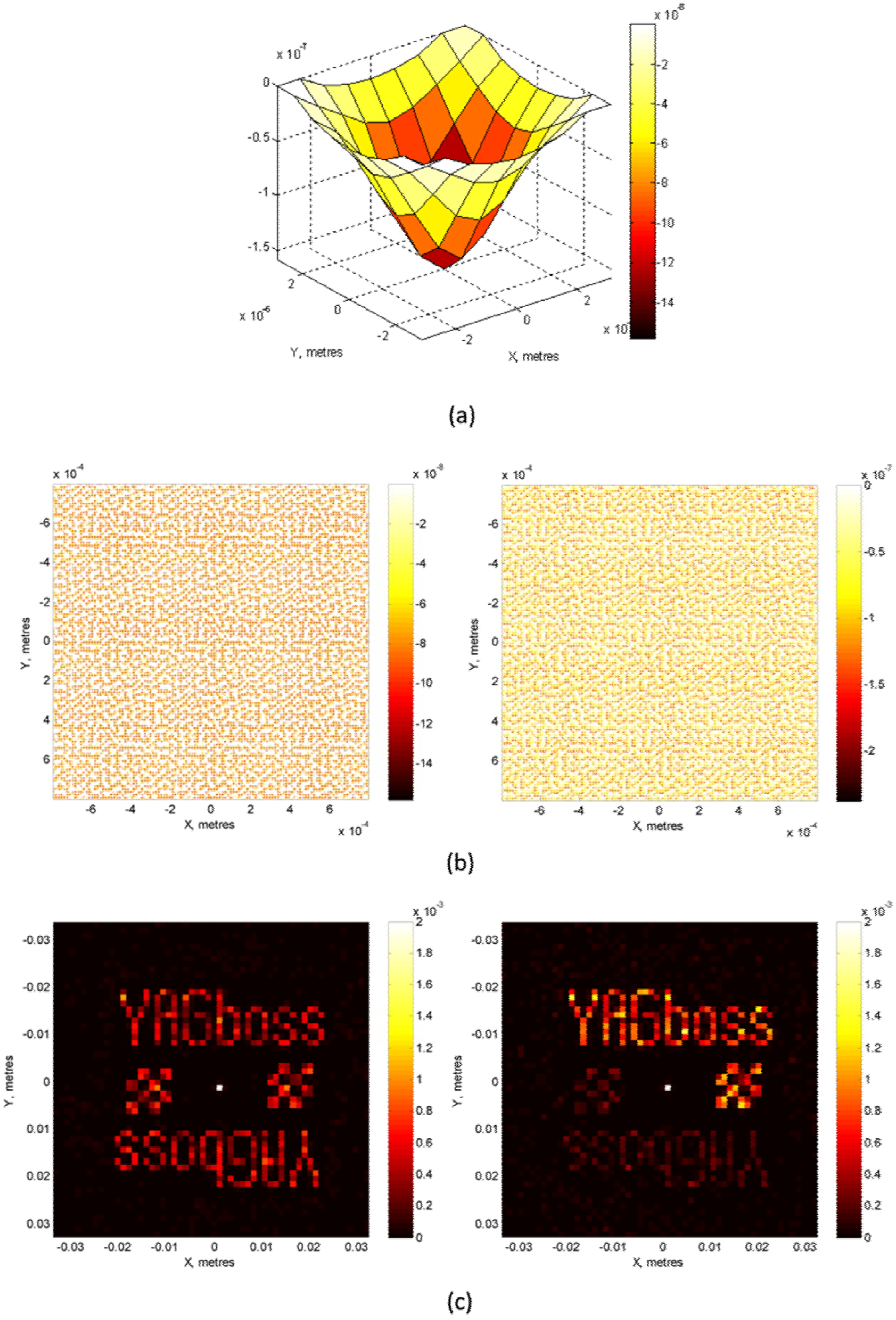

Figure 12. (a) Shape of the CGH pixel used for simulations, (b) 2-level CGH (left) and 4-level CGH (right) with the '*crater-like*' pixels, and (c) simulated diffractive image produced by the 2-level CGH (left) and 4-level CGH (right) with the '*crater-like*' pixels. The simulations were performed using the Fresnel approximation for a 1 mm dia. laser beam, $\lambda = 633$ nm and a 1 metre projecting distance. The intensity of the 0^{th} order beam was attenuated (500 times) in order to enhance the contrast ratio between the 0^{th} order beam and the diffraction image.

3.3. Fabrication process

The fabrication process of the holographic structures (security markings) on metals was performed using the optical setup shown in Figure 1. The test substrate was 304-grade stainless steel because this metal showed a good response to the 35 ns laser pulses in UV (see Section 2.2 for more details). Thanks to the precise synchronisation between the laser pulse firing and the movement of the translation stages, it was possible to perform mapping of the CGH pixels on to the metal surface with the positioning accuracy better than 0.5 µm. The 50 mm focal length of the final lens enabled the generation of '*Gaussian-like*' craters with a diameter of less than 8 µm. Although a galvo-scanner equipped with a flat-field (F-theta) lens can be used for the generation of holographic structures on the metal surface in UV, which can be beneficial in terms of the laser processing speed, this equipment was not available in our experimental laser system.

Figure 13 shows a mechanically pre-polished 304-grade stainless steel sample with a 2-level holographic structure that was generated by 35 ns laser pulses in UV. The hologram contains optically smooth craters with an average depth of 250 nm and a diameter of 7 µm. Each crater was produced by a single laser pulse of energy 2.5 µJ (i.e. a 25 mW average power and a 10 kHz pulse repetition frequency). The laser-generated hologram (security marking) contains 9 identical patterns, like those shown in Figure 12 (b), which were tiled in a 3 × 3 arrangement. The overall dimension of the hologram area was approximately 1.6 × 1.6 mm. The time required to generate the 2-level holographic structure was approximately 2 hours and 30 minutes. Such a long processing time was related to the fact that the metal workpiece was moved by the linear translation stages which required a relatively long response time to move the workpiece to the next laser firing position.

Since the laser processing time was very long, and hence such a laser system cannot be used for marking products in mass production, we also performed an experiment in which the 2-level holographic structure was generated on the surface of a 304-grade stainless steel using a 50 W HS-S SPI fibre laser that provided 220 ns pulses to the workpiece via a galvo-scanner equipped with a 160 mm FL F-theta lens at a 1064 nm wavelength. Although the 1064 nm wavelength did not provide as accurate control over the depth of the LISDs at the 343 nm wavelength, this experiment showed that it is possible to generate the 1.6 × 1.6 mm holograms in less than 20 seconds. This means that the use of a galvo-scanner with a very short focal length F-theta lens designed for UV (e.g. 03-70FT-100-355 Jenar® lens from Jenoptik AG, see: www.jenoptik.com) would significantly reduce the processing time without having a negative impact on the depth control and the diameter of the laser-generated surface features.

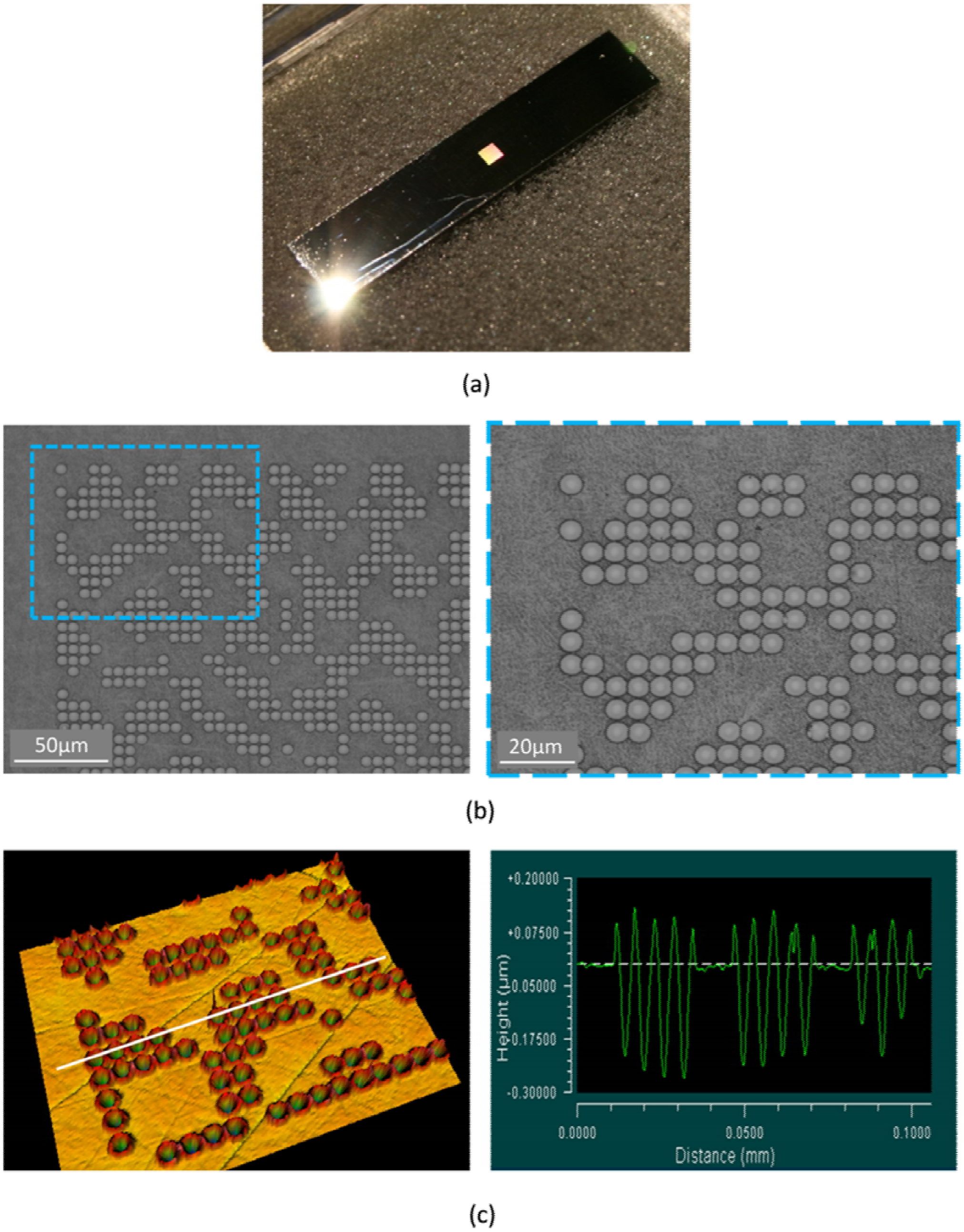

Figure 13. 2-level holographic structure (security marking) produced on the surface of a 304-grade stainless steel: (a) photograph of the metal sample with the laser-written hologram, (b) optical microscope images, and (c) surface profile measured with the Zygo® white light source interferometer.

Figure 14 shows an optical microscope image of the 4-level holographic structure, which was generated by the 35 ns laser pulses in UV, and also a surface profile of the individual hologram pixels. In order to obtain different depth of the pixels the metal surface was machined at three different pulse energies: 1.8 µJ, 2.1 µJ and 2.5 µJ. This enabled the generation of '*crater-like*' pixels with an average depth of either 175 nm, 245 nm or 290 nm.

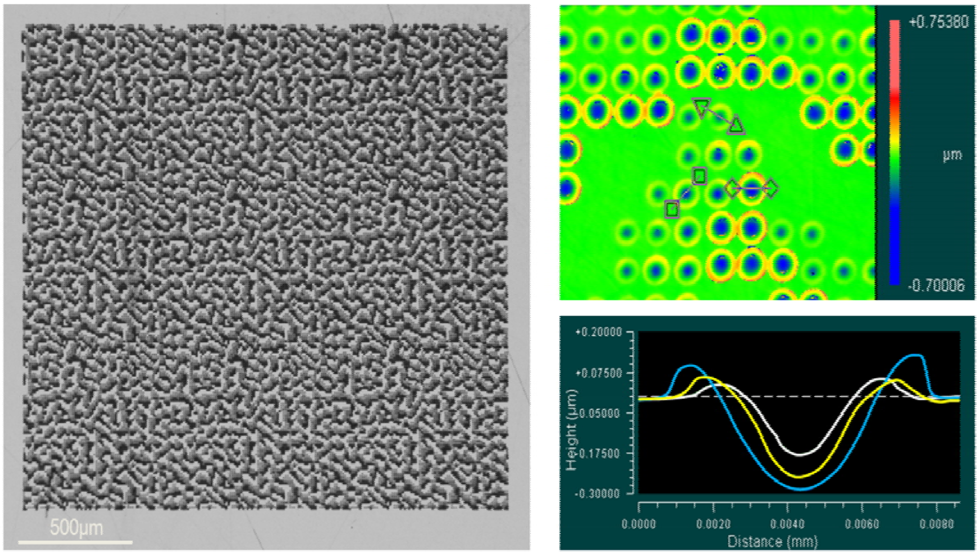

(a) (b)

Figure 14. The 4-level holographic structure generated on the surface of a 304-grade stainless steel: (a) an optical microscope image, (b) surface profile of the laser-generated pixels. The profile was measured with the Zygo® white light source interferometer.

3.4. Testing

The optical performance of the laser-generated holograms was determined by illuminating the holographic structure with a He-Ne laser beam (λ = 633 nm) and projecting the diffractive image onto a screen that was located approximately 1 metre from the hologram. This image was recorded using a digital camera.

Figure 15 shows the diffractive images produced by the 2-level and 4-level laser-generated holograms shown already in Figures 13 and Figure 14, respectively. In both cases, the incident angle of the He-Ne laser beam was approximately 10 degrees (with respect to the surface normal). The diffraction images were unchanged when the incident angle was varied between 5 and 20 degree. In general, the diffraction images are very similar to the calculated images presented in Figure 12 (c). They contain both the 0^{th} order beam and the '*twin*' image, which is less pronounced in the image produced by the 4-level hologram. The presence of the 0^{th} order beam and the '*twin*' image results from the '*Gaussian-like*' shape of the hologram pixels, as observed by performing the simulations described in Section 3.2. Although the depth of the craters in the 4-level holographic structure was not exactly the same as those used in the simulations to give the significantly suppressed '*twin*' image, it still can be seen that the multi-level laser-generated holograms have the potential to provide additional marking features for protecting high value metal products and components from counterfeiting.

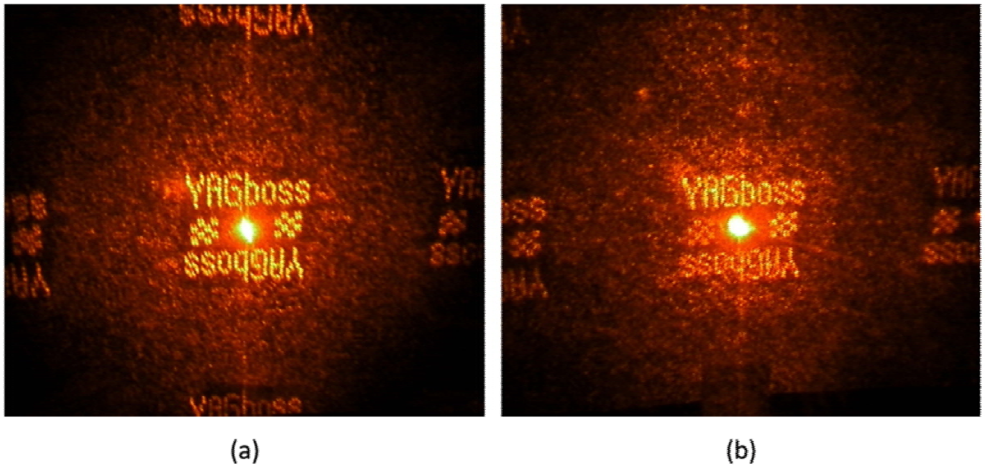

Figure 15. Diffraction image generated by: (a) 2-level hologram and (b) 4-level hologram. The holograms were fabricated using the UV nanosecond laser pulses.

4. Conclusions and future work

A novel laser-based approach for unique security marking of the high value products and components made of metals was described in this paper. It was shown that UV nanosecond laser pulses are able to locally and controllably melt the metal surface in order to generate optically smooth surface features. By arranging the laser-induced surface deformations in an appropriate pattern, it is possible to generate holographic structures that can act as security markings. Although the time required to produce the holograms in our experiments was very long (approximately 2 hours and 30 minutes), the processing time can be significantly reduced (to less than 20 seconds per hologram) by introducing a laser beam galvo-scanning system into the laser marking setup. Further work should be focused on the generation of the surface features with a square contour and a flat bottom. Our simulations described in Section 3.2 showed that the holograms with '*square pixels*' can produce diffractive images with a very high image contrast and the diffraction efficiency of more than 25%. Moreover, such holograms can produce the diffraction images without the presence of the 0th order beam and even the '*twin*' image in the case of the multi-level holographic structures. In order to generate the surface deformations with a square contour and a flat bottom, we plan to test laser mask projection techniques.

Acknowledgments

The research covered in this paper was funded by the Engineering and Physical Sciences Research Council (EPSRC), Heriot-Watt Innovative Manufacturing Research Centre (HW-IMRC, Grant No.: EP/F02553X/1) and our industrial partner Renishaw plc. (UK).

References

Beck, R.J., Parry, J.P., MacPherson, W.N., Waddie, A.J., Weston, N.J., Shephard, J.D., Hand, D.P., 2010. Application of cooled spatial light modulator for high power nanosecond laser micromachining. Opt. Express 18, 17059-17065.

Bennett, T.D., Krajnovich, D.J., Li, L., 1999. Thermophysical modelling of bump formation during CO_2 laser texturing of silicate glasses. J. Appl. Phys. 85, 153-159.

Brusasco, R.M., Penetrante, B.M., Butler, J.A., Maricle, S.M., Peterson, J.E., 2001. CO_2-Laser Polishing for Reduction of 351-nm Surface Damage Initiation in Fused Silica. In: Exarhos, G.J., Guenther, A.H., Lewis, K.L., Soileau, M.J., Stolz, C.J. (Eds.), Proceedings of SPIE 4679, Boulder, Colorado, pp. 34-39.

Chen, S.C., Cahill, D.G., Grigoropoulos, C.P., 2000. Melting and surface deformation in pulsed laser surface micromodification of Ni-P disks. J. Heat Transfer 122, 107-112.

Cheng, J., Kahlen, F.J., Kar, A. 2000. Effects of intrapulse structure on hole geometry in laser drilling. J. Laser Appl. 12, 232-238.

Cormont, P., Combis, P., Gallais, L., Hecquet, C., Lamaignère, L., Rullier, J.L., 2013. Removal of scratches on fused silica optics by using a CO_2 laser. Opt. Express 21, 28272-28289.

Dahotre, N.B., Harimkar, S.P., 2008. Laser fabrication and machining of materials. Springer, pp. 277-280.

Dai, W., Xiang, X., Jiang, Y., Wang, H.J., Li, X.B., Yuan, X.D., Zheng, W.G., Lv, H.B., Zu, X.T., 2011. Surface evolution and laser damage resistance of CO_2 laser irradiated area of fused silica. Opt. Lasers Eng. 49, 273-280.

Euastathopoulos, N., Drevet, B., Ricci, E., 1998. Temperature coefficient of surface tension for pure liquid metals. J. Cryst. Growth 191, 268-274.

Freese, W., Kampfe, T., Kley, E.B., Tunnermann, A. 2010. Design of binary subwavelength multiphase level computer generated holograms. Opt. Lett. 35, 676-678.

Goodman, J.W., 2005. Introduction to Fourier optics, third ed., Roberts & Company, Englewood, Colorado, pp. 63-96, 209-215.

Heidrich, S., Willenborg, E., Richmann, A., 2011. Development of a Laser Based Process Chain for Manufacturing Freeform Optics. Physics Procedia 12, 519-528.

Heiple, C.A., Roper, J.R. 1982. Mechanism for minor element effect on GTA fusion zone geometry. Welding J. 61, 97s-102s.

Keene, B.J., Mills, K.C., Bryant, J.W., Hondros, E.D., 1982. Effect of surface active elements on the surface tension of iron. Can. Metall. Q. 21, 393-403.

Khoong, L.E., Lam, Y.C., Zheng, H.Y., Chen, X., 2010. Laser soft marking on silicon wafer. J.Appl. Phys. 107, 053107.

Kumstel, J., Kirsch, B., 2013. Polishing titanium- and nickel-based alloys using cw-laser radiation. Phys. Procedia 41, 362-371.

Laguarta, F., Lupon, N., Armengol, J., 1994. Optical glass polishing by controlled laser surface-heat treatment. Appl. Opt. 33, 6508-6513.

Leitz, K.H., Redlingshofer, B., Reg, Y., Otto, A., Schmidt, M., 2011. Metal ablation with short and ultrashort laser pulses. Phys. Procedia 12, 230-238.

Mendez, E., Nowak, K.M., Baker, H.J., Villarreal, F.J., Hall, D.R., 2006. Localized CO_2 laser damage repair of fused silica optics. Appl. Opt. 45, 5358-5367.

Mills, K.C., Keene, B.J., Brooks, R.F., Shirali, A., 1998. Marangoni effects in welding. Phil. Trans. R. Soc. Lond. A 256, 911-925.

Monjardin, J.F., Nowak, K.M., Baker, H.J., Hall, D.R., 2006. Correction of beam errors in high power laser diode bars and stacks. Opt. Express 14, 8178-8183.

Nowak, K.M., Baker, H.J., Hall, D.R., 2006. Efficient laser polishing of silica micro-optic components. Appl. Opt. 45, 162-171.

Nusser, C., Sandker, H, Willenborg, E., 2013. Pulsed laser micro polishing of metals using dual-beam technology. Phys. Procedia 41, 346-355.

Prokhorov, A.M., Konov, V.I., Ursu, I., Mihailescu, I.N., 1990. Basic regimes of the heating of metal targets by laser irradiation. In: Pike, E.R., Welford, W.T. (Eds.), Laser heating of metals, Adam Hilger, pp.39-75.

Shiu, T.R., Grigoropoulos, C.P., Cahill, D.G., Greif, R., 1999. Mechanism of bump formation on glass substrates during laser texturing. J. Appl. Phys. 86, 1311-1316.

Stepien, P.J., 2000. Computer-generated holograms and diffraction gratings in optical security applications. In: Van Renesse, R.L., Vliegenthart, W.A. (Eds.), Proc. SPIE 3973, San Jose, pp. 224

Temmler, A., Graichen, K, Donath, J. 2010. Laser polishing in medical engineering; Laser polishing of components for left ventricular assist devices. Laser Technik J. 7, 53-57.

Temmler, A., Willenborg, E., Wissenbach, K., 2011. Design surfaces by laser remelting. Phys. Procedia 12, 419-430.

Trela, N., Baker, H.J., Wendland, J.J., Hall, D.R., 2009. Dual-axis beam correction for an array of single-mode diode laser emitters using a laser-written custom phase-plate. Opt. Express 17, 23576-23581.

Ukar, E., Lamikiz, A., Martinez, S., Estaloyo, F., Tabernero, I., 2013. Laser polishing of GGG70L cast iron with 2D scan-head. Procedia Eng. 63, 53-59.

Von Allmen, M., Blatter, A., 1995. Melting and Solidification. In: Gonser, U., Osgood, R.M., Panish, M.B., Sakaki, H. (Eds.), Laser-beam interactions with materials: physical principles and applications, Springer Verlag, pp. 68-114.

Weston, N.J., Hand, D.P., Giet, S., Ardron, M., 29 March 2012. A method of forming an optical device. Patent WO/2012/038707.

Wissenbach, K., Weisheit, A., Willenborg, E., Temmler, A., Backes, G. Gasser, A., Gottman, J., 2011. Surface treatment. In: Poprawe, R., (Ed.), Tailored light 2 – Laser application technology, RWTHedition, Springer Berlin Heidelberg, pp. 173-239.

Wlodarczyk, K.L., Mendez, E., Baker, H.J., McBride, R., Hall, D.R., 2010. Laser smoothing of binary gratings and multilevel etched structures in fused silica. Appl. Opt. 49, 1997-2005.

Wlodarczyk, K.L., Thomson, I.J., Baker, H.J., Hall, D.R., 2012. Generation of microstripe cylindrical and toroidal mirrors by localized laser evaporation of fused silica. Appl. Opt. 51, 6352-6360.

Wlodarczyk, K.L., Kaakkunen, J.J.J., Vahimaa, P., Hand, D.P., 2014. Efficient speckle-free laser marking using a spatial light modulator. Appl. Phys. A 116, 111-118.

Wyrowski, F. 1991. Upper bound of the diffraction efficiency of diffractive phase elements. Opt. Letters 16, 1915-1917.

Wyrowski, F., Bryngdahl, O., 1988. Iterative Fourier-transform algorithm applied to computer holography. J. Opt. Soc. Am. A 5, 1058-1065.

Highlights

- UV nanosecond laser pulses successfully used for precision shaping of metal surfaces
- Laser-induced surface deformations (LISDs) are optically smooth
- Shape and dimension of LISDs depend on the metal and laser processing parameters
- UV ns laser pulses are capable of producing unique security markings on metals
- The markings are embedded to the metal surface and are resistant to tampering